Research Square

Preprints are preliminary reports that have not undergone peer review.
They should not be considered conclusive, used to inform clinical practice,
or referenced by the media as validated information.

Human Adrenal Gland Charts within the Common Coordinate Framework from CT-based Imaging

Wei Liao

weiliao.wl@gmail.com

University of Electronic Science and Technology of China

Hao Tang

Jiao Li

University of Electronic Science and Technology of China

Yuxuan Qiao

Nanjing University

Lei Qiao

Nanjing University

Qiang Xu

Nanjing Jinling Hospital

Kangjia Chen

University of Electronic Science and Technology of China

Xian Zhou

Jiangsu Province Hospital of Chinese Medicine

Wenji Ni

Nanjing University

Yong Zhong

Nanjing University

Xiao Hu

The Affiliated Brain Hospital of Nanjing Medical University

Jing Sun

Nanjing University

Jianrui Li

Department of Diagnostic Radiology, Jinling Hospital, Affiliated Nanjing Medical University, Nanjing, China.

Zhiliang Long

Southwest University

Ya Liu

Nanjing University

Chen Chen

Nanjing University
Chi Zhang
Liyang People's Hospital
Hongju Wu
Nanjing University
Ming Sun
Nanjing University
Xufang Sun
Nanjing University
Yuting Feng
Nanjing University
Dan Wu
Nanjing University
Zicheng Xiong
Nanjing University
Yinghuan Shi
Nanjing University
Liang Jiang
Nanjing Medical University
Xiaoqing Cheng
Nanjing University
Xiaoping Yang
Nanjing University
Ziwei Nie
Nanjing University
Zhiqiang Zhang
Nanjing Jinling Hospital

Article

Keywords: adrenal gland, common coordinate framework, Computer Tomography, charts, statistical parametric mapping

Posted Date: March 10th, 2026

DOI: https://doi.org/10.21203/rs.3.rs-9019513/v1

License: This work is licensed under a Creative Commons Attribution 4.0 International License.
Read Full License

Additional Declarations: There is **NO** Competing Interest.

Human Adrenal Gland Charts within the Common Coordinate Framework from CT-based Imaging

Hao Tang[1]†, Jiao Li[2]†, Yuxuan Qiao[3]†, Lei Qiao[3]†, Qiang Xu[1], Kangjia Chen[2], Xian Zhou[4], Wenji Ni[5], Yong Zhong[5], Xiao Hu[6], Jing Sun[1], Jianrui Li[1], Zhiliang Long[7], Ya Liu[1], Chen Chen[1], Chi Zhang[8], Hongju Wu[1], Ming Sun[1], Xufang Sun[1], Yuting Feng[1], Dan Wu[1], Zicheng Xiong[9], Yinghuan Shi[9], Liang Jiang[10], Xiaoqing Cheng[1], Xiaoping Yang[3], Ziwei Nie[3,✉], Wei Liao[2,✉], Zhiqiang Zhang[1,9✉]

[1]Department of Radiology, Affiliated Jinling Hospital, Medical School, Nanjing University, Nanjing, China.

[2]The Clinical Hospital of Chengdu Brain Science Institute, School of Life Science and Technology, University of Electronic Science and Technology of China, Chengdu, China.

[3]School of Mathematics, Nanjing University, Nanjing, China.

[4]Health Management Center, Jiangsu Province Hospital of Chinese Medicine, Nanjing, China.

[5]Department of Health Medicine, Jinling Hospital, Affiliated Hospital of Medical School, Nanjing University, Nanjing, China.

[6]Department of Radiology, The Affiliated Brain Hospital of Nanjing Medical University, Nanjing, China.

[7]School of Psychology, Southwest University, Chongqing, China

[8]Department of Radiology, Liyang People's Hospital, Changzhou, Jiangsu Province, China.

[9]School of Computer Science, Nanjing University, Nanjing, China.

[10]Department of Radiology, Nanjing First Hospital, Nanjing Medical University, Nanjing, China.

† These authors contributed equally to this work.

✉ Corresponding authors:

Ziwei Nie (nieziwei@nju.edu.cn), Wei Liao (weiliao.wl@gmail.com), Zhiqiang Zhang (zhangzq2001@126.com)

Title character count: 76
Word count of abstract: 175
Word count of main text: 3139
Number of references: 93
Number of Table(s): 0
Number of Figure(s): 5
Supporting Material(s): 1

Abstract

The human adrenal gland is a critical endocrine organ that regulates physiological processes and modulates diseases progressions. However, the extent to which adrenal gland morphometrics vary by age, sex, and pathological conditions remains limited due to challenges with the adrenal gland template. Based on large cohorts (total *N* = 37,251) of adrenal CT, we developed artificial intelligence-enabled methods to construct an adrenal gland common coordinate framework and to provide morphological and densitometric templates for voxel-wise statistical parametric mapping analysis. We delineated sex-stratified developmental trajectories of adrenal imaging metrics across 18 to 100 years. Adrenal developmental trajectories derived from CCF-based analysis, which was validated by conventional regional analysis, showed distinct sex-specific patterns: an inverted-U shape in males and a gradual age-related increase in females. We mapped topographic patterns of the adrenal gland associated with physical/physiological measures and changes in four adrenal gland-related pathological conditions. Our findings provided a quantitative spatial reference system for comparing and correlating bilateral adrenal gland data from multiple individuals and conditions, thereby facilitating novel insights into its physiology and pathophysiology.

Keywords: adrenal gland, common coordinate framework, Computer Tomography, charts, statistical parametric mapping,

Introduction

The human adrenal gland is a critical neuroendocrine organ located retroperitoneally superior to both kidneys. Anatomically, it consists of a body, a medial limb, and lateral limbs[1]. Although small in size and anatomically unimposing, it regulates a wide array of physiological functions[2, 3] and is implicated in the pathogenesis of numerous diseases[4-6]. Histologically, the outer cortex secretes mineralocorticoids and glucocorticoids, which regulate water-electrolyte balance and glucose-lipid metabolism, and form part of the hypothalamic-pituitary-adrenal axis that mediates stress responses and modulates immunity[7, 8]. In contrast, the inner medulla secretes epinephrine and norepinephrine, which regulate blood pressure and heart rate in response to sympathetic activation[9, 10].

Computed Tomography (CT)-imaging is the primary non-invasive approach for current assessment of the adrenal gland[11-15]. Morphometric measurements of the adrenal gland not only constitute the foundation of clinical radiological diagnosis[16-19], but also act as critical indicators in studies of metabolic, immune, stress-related disorders, and psychiatric and psychological diseases[20-22]. Therefore, establishing and validating normative references for imaging parameters is an essential prerequisite for quantitative adrenal analysis[23]. As with other human organs, the morphological features of the normal adrenal gland are closely linked to an individual's physical conditions and demographic characteristics. A systematic analysis of these factors, particularly the establishment of normative charts[24-28] illustrating age-related alterations in adrenal morphology across the lifespan, is crucial for developing more accurate, age-specific references for quantitative imaging measurements of the adrenal gland[29]. Moreover, this would enhance insights into the physiological processes underlying adrenal development and aging.

Conventional morphological imaging assessment of the adrenal gland has largely relied on simple manual size measurements using predefined regions/lines of interest[30-32]. The approach is prone to substantial subjective bias, time-consuming, and labor-intensive, rendering it suitable only for small-sample data analysis. With the

advancement of artificial intelligence (AI)-assisted automatic image segmentation techniques[33], recent studies have adopted indices such as total adrenal surface area or volume[34-36], which can reflect glandular morphological features more objectively and stably with high test-retest reliability[37, 38]. However, such individual space-based measurements are limited by a paucity of indices and fail to comprehensively capture the complex morphological information of the adrenal gland, particularly the region-specific physiological or pathological characteristics of distinct adrenal zones[39, 40]. Different regions of the adrenal gland exhibit marked heterogeneity in histological structure, physiological function, and the pathological correlates of associated diseases[41-45], highlighting the inherent limitations of traditional measurement methods.

The voxel-based analysis strategy based on a common coordinate framework (CCF) effectively overcomes the aforementioned limitations in quantitative imaging measurements of organs[46-48]. Originating in stereotactic neurosurgery[49], this strategy has become the foundational technique for current brain imaging[50]. Its core principle involves realigning individual brains to a common standard space to achieve precise, quantified coordinate locations for each brain structure/voxel[51]. Subsequently, this voxel-wise statistical analysis is ready to correlate demographic, clinical, or behavioral variables with imaging parameters, generating statistical parametric maps[52]. This method enables automatic, comprehensive, and intuitive visualization of organ spatial features without prior assumptions[53]. Furthermore, leveraging sophisticated image processing techniques, it can be extended to diverse visualization ways, including surface- and atlas-based representations[54, 55]. Critically, the CCF strategy lays a space-shared platform for multimodal data fusion analysis[47, 56, 57] and provides the essential coordinate information for spatial transcriptomics of the Allen Human Brain Atlas[58]. Inspired by brain imaging studies, the CCF-based statistical parametric mapping strategy has recently been extended to somatic organs, including the heart[59], lungs[60], thymus[61], and whole-body[62, 63], enabling detailed characterization of functional, physiological, and pathological features across anatomical regions of these organs. This approach also constitutes the core methodological basis of the NIH Whole-Body CCF-HuBMAP Project[64-66]. Therefore, the development of a novel CCF specifically for

the adrenal gland is of great theoretical and practical significance.

Against this background, we enrolled high-resolution CT data from healthy participants (*N* = 35,751) and individuals with four pathological conditions (*N* = 8,227). We developed AI-enabled methods to align individual adrenal CT images into a 3D adrenal CCF, enabling voxel-based statistical parametric mapping. This framework allows for the precise characterization of spatially location-specific tissue, functional, and pathological features of the adrenal gland without prior assumptions. Concurrently, we established normative references for morphometric (i.e., volume) and densitometric (i.e., density) measurements of the adrenal gland in the common space and benchmarked the individual developmental trajectories against rich biological information. Looking forward, it also paved the methodological way for integrating the adrenal gland into the currently prevalent multi-organ CCF analysis and spatial multi-omics research.

Results

After rigorous quality control (Fig. S1), the healthy cohort (cohort 1, *n* = 12,319) was used to train the AI segmentation model, construct templates, and generate normative charts. The pathological cohort (cohort 2, *n* = 2,907) was used to investigate disease-related alterations in adrenal imaging metrics (Figure 1).

Imaging metrics and templates for CT-based adrenal CCF

AI-enabled adrenal segmentation was performed using the nnU-Net framework. The nnU-Net model achieved mean Dice scores of 0.95 ± 0.02 (5-fold cross-validation, *n* = 250), 0.94 (interquartile range, IQR: 0.90-0.98) on an internal test set (*n* = 50), and 0.92 (IQR: 0.89-0.95) on the public BTCV dataset (*n* = 30)[67]. After normalization, we obtained two parameters from each individual: the Jacobian determinant (JD), which characterized the degree of non-linear stretching and deformation warping from individual space to the standard template space and served as a voxel-wise morphometrical metric (volume)[68]; the CT intensity value in Hounsfield units (HU) within the standard space, served as a voxel-wise densitometric metric (density).

The density map of each adrenal gland across 1,338 participants within the CCF (64 mm × 64 mm × 64 mm bounding box, with the original point at the image centroid) was averaged and used as the template for adrenal CT (Figure 2a). The mean density map showed a spatially heterogeneous pattern, with higher values in the inner regions and lower values in the outer regions. A binary mask was provided (Figure 2b). These templates are available at https://github.com/weiliao81/Adrenal-gland-CCF.

Charting and statistically mapping the adrenal gland across the lifespan and between sexes

To establish normative references for quantitative imaging measurements and to develop benchmark developmental trajectories of the adrenal gland, we charted adrenal gland metrics across participants (*n* = 10,681, aged 18-100 years) and between sexes. For morphological metrics, males had larger adrenal glands than females. The lifespan trajectories of global adrenal gland size in males exhibited an inverted U-shape: volume increased nonlinearly from age 18, peaked in the late fifth to early sixth decade, and then declined nonlinearly thereafter. In contrast, adrenal gland size in females increased monotonically with advancing age (Figure 3a). For density metrics, the trajectory patterns in both sexes were similar to those of morphological metrics. Still, in the opposite direction: with increasing age, males displayed a U-shaped pattern bottomed in the late fifth to sixth decade, whereas females showed a monotonic decrease (Figure 3b). Moreover, males had lower adrenal gland density than females at most ages. We further performed atlas-based imaging metric analysis of the adrenal gland in different inner (Left: 715 mm^3; Right: 617 mm^3) and outer (Left: 3970 mm^3; Right: 3332 mm^3) regions. Trajectories in the inner region showed patterns similar to those of the whole adrenal gland described above (Fig. S2).

To verify the validity of the CCF-based results, we next performed comparative and correlation analyses against metrics obtained using the conventional ROI-based strategy in the native space. We found that the trajectory profiles derived from the two strategies were nearly identical. In addition, strong correlations were also observed for both volume (Left: $R = 0.999$, $P < 0.0001$; Right: $R = 0.998$, $P < 0.0001$)

and density (Left: $R = 0.979$, $P < 0.0001$; Right: $R = 0.977$, $P < 0.0001$) metrics between the two measurement strategies (Fig. S3).

We further used voxel-based analysis (VBA) to demonstrate the sex-specific topographic characteristics of adrenal gland metrics. Consistent with the previous findings in the charts, males exhibited a larger volume than females; whereas males showed higher density in the inner region and lower density in the outer region relative to females ($P_{FDR} < 0.05$ with False Discovery Rate correction, Figure 3c & d).

Topographic patterns of adrenal metrics associated with physical/physiological measures

To investigate the association between adrenal imaging metrics and physical/ physiological indicators, we applied our CCF-based VBA correlation analysis to healthy adrenal datasets (n = 10,681). We included those with available data on body mass index (BMI), red blood cell count (RBC), neutrophil-to-lymphocyte ratio (NLR), and heart rate (HR) (Table S2). Statistical parametric mapping revealed significant correlations between adrenal imaging metrics and each of the physiological parameters examined. For BMI of physical indicator, bilateral adrenal glands showed consistent positive correlations with global volume (Left: $R = 0.47$, $P_{FDR} < 0.0001$; Right: $R = 0.45$, $P_{FDR} < 0.0001$) and negative correlations with density (Left: $R = -0.38$, $P_{FDR} < 0.0001$; Right: $R = -0.31$, $P_{FDR} < 0.0001$) (Figure 4a & e). For the neutrophil-to-lymphocyte ratio, a marker of systemic inflammatory and immune status, positive correlations were observed with bilateral adrenal volume (Left: $R = 0.10$, $P_{FDR} < 0.0001$; Right: $R = 0.07$, $P_{FDR} < 0.0001$), whereas no significant associations were detected for density metrics (Figure 4b & f). The indicator of red blood cell count was positively correlated with volume in the right adrenal outer region ($R = 0.03$, $P_{FDR} = 0.004$) (Figure 4c) and with density in the inner region of both the left and right adrenal glands (Figure 4g). Heart rate, a measure closely linked to adrenal medullary function, was indeed positively correlated with volume metrics in the adrenal inner region (Left: $R = 0.04$, $P_{FDR} = 0.003$; Right: $R = 0.04$, $P_{FDR} = 0.003$), whereas no significant associations were detected for density metrics (Figure 4d & h).

Topographic patterns of adrenal metrics associated with pathological conditions

We profiled adrenal imaging metrics in participants with four pathological conditions (total n = 2,907, Tables S2). Applying our CCF-based VBA approach, we identified distinct topographic patterns of imaging metric alterations associated with each condition. Compared with healthy controls (HCs), individuals with hypertension (HTN) exhibited globally increased adrenal volume (Left: $t_{(10,677)} = 15.87$, $P_{FDR} < 0.0001$; Right: $t_{(10,677)} = 19.85$, $P_{FDR} < 0.0001$), together with elevated inner region density and reduced outer region density (Figure 5a & e). Individuals with inflammatory bowel disease (IBD), an autoimmune disorder, showed increased bilateral adrenal volume (Left: $t_{(1250)} = -5.57$, $P_{FDR} < 0.0001$; Right: $t_{(1250)} = -8.99$, $P_{FDR} < 0.0001$) and decreased density in the right adrenal gland ($t_{(1250)} = 14.80$, $P_{FDR} < 0.0001$) (FDR-correction with $P < 0.05$) (Figure 5b & f). Individuals with stroke, representing acute stress, displayed enlarged bilateral adrenal volume (Left: $t_{(470)} = 2.70$, $P_{FDR} = 0.01$; Right: $t_{(470)} = 2.75$, $P_{FDR} = 0.01$) and increased density in the right adrenal gland($t_{(470)} = 2.81$, $P_{FDR} = 0.009$) (Figure 5c & g). In individuals with major depressive disorder (MDD), most regions of the adrenal gland showed reduced volume (Left: $t_{(959)} = -2.03$, $P_{FDR} = 0.05$; Right: $t_{(959)} = -5.58$, $P_{FDR} < 0.0001$) and increased density (Left: $t_{(959)} = 5.68$, $P_{FDR} < 0.0001$; Right: $t_{(959)} = 16.05$, $P_{FDR} < 0.0001$) (Figure 5d & h). Notably, in the latter three diseases, the left adrenal gland consistently exhibited distinct inner-outer layer dissociation in density metrics (Figure 5f-h).

Discussion

Leveraging large-scale CT images from healthy individuals and cutting-edge AI-assisted image segmentation, we established, for the first time, the morphological and densitometric characteristics of the adrenal gland with CCF. The development of adrenal CCF addressed the technical constraints inherent to traditional region-, volume-, or line-of-interest-based morphometric measurements, enabling voxel-based statistical parametric mapping of the adrenal glands and laying a pivotal foundation for integrating the adrenal glands into prevailing CCF-based multi-organ and spatial multi-omics workflows[46, 59-61]. By charting the adrenal metrics across the

lifespan within CCF, we systematically characterized sex-specific and age-related trajectories of adrenal volume and density. These norms furnished a holographic, high-resolution quantitative reference standard for clinical diagnosis of adrenal abnormalities, and advanced our understanding of the developmental and senescence characteristics of the adrenal gland. The preliminary validation of extended applications demonstrated that the established adrenal CCF and imaging norms could accurately characterize anatomical spatial specializations of the adrenal glands across demographic variables, physical and physiological parameters, and pathological conditions. This confirmed the framework's exceptional stability and reproducibility, while underscoring its considerable translational potential. Collectively, these findings not only advanced the standard space research paradigm for adrenal imaging but also highlighted broad utility in clinical diagnostic support, population health surveillance, and translational medical research.

We first constructed an adrenal gland-specific CCF, representing another organ-specific CCF developed following the extension of stereotaxic brain imaging techniques[69] to the heart, lungs, thymus, and whole-body applications[59, 61-63, 67]. For the adrenal CCF construction, we used clinically available thin-slice CT images, which offer superior spatial resolution compared to body MRI (typically limited by thicker slices and motion artifacts). This feature enables high-precision anatomical delineation of the small and complex adrenal glands. During template construction, we employed a two-step registration approach that integrates both contour and intensity information[70, 71], guided by a high-performance AI segmentation model validated against expert manual annotations. In addition to a morphological template for Jacobian deformation/volume quantification in standard space, we also generated a density template to facilitate quantitative assessment of adrenal gland density, which is challenging to measure manually due to its small size and complex geometry[30, 72]. Importantly, the adrenal CCF enables precise localization of adrenal anatomical landmarks and supports voxel-wise quantitative analysis, thereby establishing a methodological foundation for potential studies with CCF-based multi-organ[73-75] and spatial multi-omics investigations[64] of the adrenal gland.

Using the adrenal CCF, voxel-wise statistical parametric mappingrevealed spatial/anatomical specialization features of the adrenal gland in both morphology and density, corresponding to histological, physiological, and pathological phenotypes. The topographic patterns varied across these phenotypic traits. These exploratory findings demonstrated the advantages of voxel-based approaches, which operate without a priori anatomical assumptions, in contrast to conventional ROI-based methods that only report summary statistics within predefined regions[76].

Using a large imaging dataset of healthy individuals covering a wide age range, we constructed the first voxel-wise 3D normative models for adrenal morphology and density in a standard stereotaxic space. We specifically quantified sex- and age-related differences in adrenal volume and density. Both VBA and ROI analyses revealed that males had relatively larger adrenal volumes and lower density values than females. Lifespan trajectory analysis demonstrated an inverted U-shape volume trajectory in males, consistent with previous reports[24, 35]. However, we observed a monotonically increasing volume trajectory across the lifespan in females, which diverges from the U-shaped pattern previously described[41, 77, 78]. Methodological bias was unlikely given consistent findings across bilateral adrenal glands and strong concordance between voxel-wise and ROI-based measurements. Previous histological studies[77, 79] link female adrenal aging to preserved glomerulosa function, fasciculata expansion, and longer telomeres. Male adrenal decline involves glomerulosa atrophy and fasciculata cell loss from telomere shortening. Developmental programming[80] traces this sex difference to intrauterine origins, sustained by hormone pathways.

We further reported the first comprehensive lifespan charts for adrenal density. Males exhibited a U-shaped density trajectory, whereas females showed a monotonic decline with age. Density changes reflect histology: decreased density from fasciculata expansion, increased density from glomerulosa/reticularis atrophy. Female monotonic decline indicates predominant fasciculata expansion. A male U-shaped trajectory suggests that post-midlife atrophy of the glomerulosa/reticularis exceeds fasciculata compensation. In contrast, the normative reference[24], our normative models based on three-dimensional images contain rich biological information,

providing a high-precision quantitative reference standard for quantitative radiological diagnosis and scientific investigation of adrenal pathophysiology.

To evaluate translational utility, we applied CCF-based voxel-wise analysis across diverse clinical and research contexts. The resulting statistical maps revealed distinct and spatially heterogeneous topographic profiles across conditions. In healthy individuals, we systematically examined the effects of four key physiological variables on adrenal morphology. The BMI was positively associated with adrenal volume and negatively associated with density, consistent with prior evidence[81, 82]. We newly identified a positive correlation between peripheral blood neutrophil-to-lymphocyte ratio—a marker of systemic immune tone—and adrenal volume[83]. Red blood cell count showed divergent associations with adrenal density: positive in the outer region and negative in the inner region, suggesting region-specific hormonal regulation of erythropoiesis by the adrenal gland[10]. Heart rate, an index of cardiac autonomic function, was positively associated with adrenal volume. Collectively, these findings aligned with well-established physiological models of adrenal function.

We further applied the CCF-based VBA framework to four representative pathological conditions closely linked to adrenal function. Hypertension was associated with global adrenal enlargement and opposing density changes in the inner and outer layers, consistent with adaptive adrenal modulation in cardiovascular dysfunction[84]. Stroke, a prototypical model of severe acute stress, was accompanied by increased adrenal volume. In contrast, inflammatory bowel disease (a form of autoimmune enteritis) and depression (a major psychiatric disorder) were associated with reduced adrenal volume. With high statistical power, the present findings corroborated previous evidence suggesting that depression may be accompanied by enlarged adrenal volume[85-87].

Density mapping revealed divergent patterns between the left and right adrenal glands across pathological states. The right adrenal gland generally showed increased density, whereas the left gland exhibited bidirectional changes, with reduced density in the inner portion and elevated density in the outer portion. These observations

support the presence of functional and histological heterogeneity within and between adrenal glands[40, 43, 44]. Notably, spatial pattern clustering across phenotypes demonstrated distinct imaging signatures between the inner and outer adrenal compartments, suggesting that CCF-based voxel-wise analysis can effectively resolve histological features of the adrenal cortex and medulla—although future histological validation remains necessary to confirm this inference. Overall, the CCF-based VBA approach demonstrated strong robustness and reliability, with substantial translational potential for advancing adrenal imaging research.

Despite these intriguing findings, several limitations should be acknowledged. First, the study population consisted solely of individuals aged 18 years and older, thereby precluding evaluation of earlier developmental stages. Second, the dataset was predominantly obtained from hospitals in China, potentially limiting the generalizability of the results. Further validation across more diverse populations—along with the incorporation of detailed ethnicity data not available in the current datasets—will be critical for establishing globally applicable reference standards. Finally, future studies using histological data as the gold standard are needed to verify the topographic patterns of the adrenal gland identified in this work.

In conclusion, our study established the adrenal-specific CCF for the first time, enabling the application of advanced voxel-wise statistical parametric mapping techniques to investigate region-specific physiological- and disease-related characteristics of the adrenal gland. It also paved the methodological way for integrating the adrenal gland into the currently prevalent multi-organ CCF analysis and spatial multi-omics research. The charts of the adrenal gland across the lifespan, based on large-scale, high-resolution CT data, defined a three-dimensional normative reference for quantitative adrenal imaging measurements and provided a benchmark for individual developmental trajectories. Further preliminary applications of the CCF-based analyses revealed a variety of novel topographic patterns corresponding to physiological and pathophysiological phenotypes of the adrenal gland, thereby providing new insights into adrenal physiology and pathophysiology.

Methods

Participants and CT imaging

This retrospective study was approved by the Ethics Committee of Jinling Hospital, Affiliated Hospital of Medical School, Nanjing University, and Jiangsu Province Hospital of Chinese Medicine, respectively, with a waiver of informed consent (Approval No. 2024DZKY-021-01).

Healthy cohort

The healthy cohort (cohort 1) initially comprised individuals (N = 35,751) who underwent non-contrast chest CT scanning for physical examination. They were consecutively selected from Affiliated Jinling Hospital, Medical School of Nanjing University (Center NJU), and Jiangsu Provincial Hospital of Chinese Medicine (Center JSHTCM) between January 2019 and December 2024. Demographic characteristics, anthropometric measures, resting heart rate, history of hypertension, and peripheral blood cell counts were collected. Participants were excluded if they had a major disease history, imaging/functional adrenal abnormalities, or glucocorticoid use within six months. Furthermore, participants were excluded if their CT images had incomplete adrenal coverage, poor adrenal contours, failed auto-segmentation, or failed image normalization. The inclusion criteria were presented in Supplementary Methods. Finally, 12,319 healthy participants remained (Fig. S1, and Table S1). Out of the cohort 1, 300 participants were used to develop an adrenal-specific AI segmentation model (Figure 1, *Segmentation* panel in "CCF assembly"); 1,338 participants as queries were used to construct a three-dimensional standard adrenal template (Figure 1, *Template* panel in "CCF assembly"); 10,681 subjects were used to depict age-related changes in adrenal gland morphometrics (Figure 1, *Normalization and SPM* panel in "CCF assembly").

Pathological cohort

The pathological cohort (cohort 2) comprised four pathological conditions (*N* = 8,227), including individuals with HTN (*n* = 2010), acute ischemic stroke (less than 7days after onset) (*n* = 500), and IBD (*n* = 500) collected from Jinling hospital, and individuals with MDD (*n* = 500) from Nanjing Brain hospital (Fig. S1). In addition, for comparative

analysis, twice as many age- and sex-matched healthy controls were selected from the health cohort as were in each condition group (Table S2). The diagnosis of participants with pathological conditions were described in Supplementary Methods.

CT imaging acquisition

All CT images were acquired from 9 64-slice CT scanners from 5 vendors, including General Electric Company, Siemens, Unite imaging, Anke, and Neusoft Medical Systems. All image data were visually inspected and quality-controlled by three experienced radiologists. All images were acquired using the following protocols: 512 × 512 matrix, field of view 40cm × 40cm; slice thickness of 1.0 mm or 1.25 mm with a reconstruction interval equal to the slice thickness (no gap); tube voltage of 120 kV or 130 kV, automatically modulated tube current. The detailed information is presented in Table S3.

CCF assembly

Image preprocessing

To ensure spatial consistency across all images, each CT volume was resampled to 1.0 mm isotropic voxels using cubic B-spline interpolation implemented with the SimpleITK library (v2.2.0).

Automated adrenal segmentation

Artificial intelligence-enabled adrenal segmentation was performed using the nnU-Net framework[88]. To generate high-quality training labels, we developed a rigorous two-tier annotation protocol. All annotators participated in a consensus-building session led by a senior radiologist to review representative cases and agree on a detailed segmentation guideline that explicitly defined the adrenal gland's boundaries relative to surrounding structures. First, the entire 3D mask of both adrenal glands on non-contrast CT images (n = 250) was independently manually annotated by two board-certified radiologists (each with 5 years of post-residency experience) using ITK-SNAP software (v4.0.1). Subsequently, a senior radiologist (with 10 years of experience) reviewed all masks, resolved discrepancies in accordance with the established guideline, and made final adjustments. This senior-arbitrated set of

segmentation masks served as the definitive ground truth.

An nnU-Net model was trained on this dataset with corresponding segmentation masks by a 5-fold cross-validation strategy (Dice scores: 0.95 ± 0.02). On an external testing dataset of 50 cases, the model achieves a mean Dice score of 0.94 with an interquartile range of [0.90, 0.98]. Besides, taking the public BTCV dataset[67] of 30 cases as an independent test set, the model achieves a mean Dice score of 0.92 with an interquartile range of [0.89, 0.95]. All model training, validation, and testing were performed on a single NVIDIA A100 with 40GB of VRAM.

Standard Template Construction

A multi-stage iterative optimization strategy was employed to construct a standard space template. The core pipeline consisted of four stages:

Initialization: An individual scan (I_0) with typical anatomical features was selected by a radiologist as the initial image template (T_0), and its corresponding organ mask (M_0) was used as the initial mask template.

Iterative registration: During the *k*-th iteration, a two-level registration was performed for each scan (I_i). Mask-guided pre-registration (rigid): The individual mask (M_i) was aligned to the current mask template (M_{k-1}) via an affine transformation to generate an initial deformation field ($\emptyset_i affine$). Mask-driven symmetric normalization (SyN) registration (non-rigid): Based on the pre-registration result, the SyN algorithm[89] was applied for non-rigid fine registration to generate the final deformation field ($\emptyset_i$).

Template update: The deformation field ($\emptyset_i$) was applied to warp all individual scans (I_i) and their masks (M_i) into the standard space, resulting in I_i^w and M_i^w. A new image template (T_k) and mask template (M_k) were generated by voxel-wise arithmetic averaging of the registered image set (I_i^w):

$$T_k(x) = \frac{1}{n}\sum_{i=1}^{N} I_i^w(x)$$

$$M_k(x) = \frac{1}{n}\sum_{i=1}^{N} M_i^w(x)$$

where *n* is the sample size. The mask template M_k was binarized using a threshold of 0.3 to ensure topological integrity.

Convergence Criterion: The normalized mean squared error (NMSE) between templates from consecutive iterations was calculated:

$$\varepsilon_k = \frac{\sum[(T_k(x) - T_{k-1}(x))^2]}{|\Omega|}$$

where Ω denotes the template spatial domain and $|\Omega|$ is the total number of voxels within the domain. The iteration terminated when $\varepsilon_k < 10^{-5}$; otherwise, T_k and M_k were used as the new templates for the next optimization cycle. The final left adrenal template converged after 8 iterations, and the right adrenal template after 6 iterations.

Spatial Normalization

A two-stage normalization pipeline was used to warp individualized adrenal gland images into a common space using the ANTs platform. Before registration, the mean CT density (HU) within the adrenal mask was computed in native space for each subject. After non-linear registration to the common template, each subject's CT image was resampled into template space. A single, binary adrenal mask derived from the standard template (template_mask) was used as a uniform region of interest to extract the meanHU value from each warped image, ensuring anatomically comparable measurements across the entire cohort. The normalization included (i) mask-based rigid registration for initial global alignment, (ii) mask-driven symmetric normalization (SyN) deformable registration for fine-scale, non-linear anatomical correspondence. Mean squared error served as the similarity metric for optimization. This mask-prioritized, hierarchical approach is more robust for adrenal morphology than affine-only registration, as it ensures anatomical shape alignment.

From the native segmentations, the absolute volume (ml) of the whole gland was computed. To assess localized volumetric differences, the JD field was derived from the individual-to-template deformation field. The JD quantifies the local volume change relative to the template (JD > 1 indicates local expansion, JD < 1 indicates local contraction, and JD = 1 indicates volume preservation). Subsequently, a voxel-wise general linear model (GLM) was applied within the template space to analyze the association between the local JD value and the observational variable, thereby identifying regions of significant morphological alteration. For subsequent analysis, we harmonized adrenal gland morphometrics using ComBat harmonization[90], to minimize scanner and protocol parameters across sites.

Applications of the adrenal template

Age chart of the adrenal gland

We performed the GAMLSSS procedure [26, 28] with adrenal gland morphometry as the dependent variable, age as a smoothing term (using a B-spline basis function), and scanner sites as random effects for males and females, respectively. The Johnson's Su (JSU) distribution, which has four parameters: median (μ), coefficient of variation (σ), skewness (γ), and kurtosis (τ), was chosen to fit the data distribution. Each adrenal gland morphometric, denoted by y, was modeled according to equations:

$$Y(i) = JSU(\mu_i, \sigma_i, \nu_i, \tau_i)$$

According to previous studies[91, 92], we fitted three GAMLSS models with different degrees of freedom (*df* = 3-5) for the B-spline basis functions in the location (μ) parameters. We set default degrees of freedom (*df* = 3) for the B-spline basis functions in the scale (σ) parameters. Following the practice of previous studies[91], only an intercept term was included for the ν or τ parameter. For model estimation, we used the default convergence criterion of log-likelihood = 0.001 between iterations and set the maximum number of iterations to 200. Finally, the optimal model for a given functional metric was selected as the one with the lowest Bayesian information criterion among all converging models.

Sex difference in the adrenal gland

For comparisons between males and females in adrenal gland density and volume, we used a two-sample t-test with age and BMI as covariates *per* voxel. The results were corrected by FDR with $p < 0.05$.

Correlation between adrenal metrics and physical/Physiological measures

To investigate the relationship between adrenal gland density and volume and physical/physiological measures, we conducted a GLM analysis at the global and voxel scales. In GLM for BMI, age and sex were considered as covariates. In GLM for HR, NLR, and RBC, age, sex, height, and weight were considered as covariates. Results are visualized using scatterplots with fitted curves for quantitative trends and thresholded statistical parametric maps for spatial effects.

Comparisons of adrenal metrics between Pathological states

To investigate differences in adrenal gland density and volume between pathological conditions and HCs, we used two-sample *t*-tests at the global and voxel scales. To minimize confounding effects, all pathological individuals were strictly matched with HCs at a 1:2 ratio based on sex and age (with no significant age difference between the groups). No individuals were reused across comparisons. Age and sex were further included as covariates in the statistical model. All results were corrected by FDR with $P < 0.05$.

Phenotyping clustering

To delineate the internal structural correspondence with imaging phenotypes, we finally performed unsupervised clustering on both adrenal glands using the scikit-learn library (v1.3.0). The number of clusters for this data-driven approach was informed by the spatial distribution patterns observed in preliminary experiments. It was set to four, corresponding to the canonical anatomical zonation (zona glomerulosa, zona fasciculata, zona reticularis, and medulla)[93].

Data availability

The public BTCV dataset is available at https://github.com/openmedlab/Awesome-Medical-Dataset/blob/main/resources/BTCV.md. Adrenal gland templates are available at https://github.com/weiliao81/Adrenal-gland-CCF.

Code availability

The software toolkits utilized in this study, including nn-Unet (https://github.com/MIC-DKFZ/nnUNet), SimpleITK (v2.2.0) (https://simpleitk.org/), ITK-SNAP (v4.0.1) (https://www.itksnap.org/pmwiki/pmwiki.php), ANTs (https://github.com/ANTsX/ANTs), GAMLSS (https://www.rdocumentation.org/packages/gamlss/versions/5.4-12/topics/gamlss).

Acknowledgments

This work was supported by the National Key Research and Development Program of China (2018YFA0701703), National Natural Science Foundation of China (82371953, 62571105, 62473082, 82121003, and 62036003), National Science and Technology Innovation 2030-Neuroscience and Brain like research (2022ZD0211800), the Sichuan Science and Technology Program (2026NSFSCZY0055, and 2026NSFSC0377), and the Fundamental Research Funds for the Central Universities (ZYGX2024XJ054).

Ethics declarations

Competing interests

The authors declare no competing interests.

Author information

Contributions

H.T., J.L., X.-Q.C., X.-P.Y., Z.-W.N., W.L., and Z.-Q.Z. conceived and designed the study. H.T., Y.-X.Q., L.Q., Q.X., K.C., X.Z., W.-J.N., Y.Z., X.H., J.S., J.-R.L., Y.L., C.C., C.Z., H.-J.W., M.S., X.-F.S., Y.S., Y.-T.F., D.W., Z.-C.X., L.J., X.-Q.C. and Z.-Q.Z. collected the data. H.T., Y.-X.Q., L.Q., and Z.-W.N. developed the AI-based automated analysis pipeline. H.T., J.L., Y.-X.Q., L.Q., Q.X., Z.-L.L., Z.-W.N., W.L., and Z.-Q.Z. contributed to the validation

analyses. H.T., and Y.-X.Q. W.L., and Z.-Q.Z. contributed to the results interpretation. H.T., J.L., J.C. and Y.-X.Q. prepared the figures and wrote the paper. Z.-W.N., W.L., and Z.-Q.Z. critically revised the manuscript. All authors reviewed and approved the final version.

Appendix A. Supplementary material

Supplementary data associated with this article can be found online.

References

1. Miller, W. L. & White, P. C. History of adrenal research: From ancient anatomy to contemporary molecular biology. *Endocr Rev* **44**, 70-116 (2023).
2. Dum, R. P., Levinthal, D. J. & Strick, P. L. Motor, cognitive, and affective areas of the cerebral cortex influence the adrenal medulla. *Proc Natl Acad Sci U S A* **113**, 9922-9927 (2016).
3. Dum, R. P., Levinthal, D. J. & Strick, P. L. The mind-body problem: Circuits that link the cerebral cortex to the adrenal medulla. *Proc Natl Acad Sci U S A* **116**, 26321-26328 (2019).
4. Vaidya, A., Findling, J. & Bancos, I. Adrenal insufficiency in adults: A review. *JAMA* **334**, 714-725 (2025).
5. Nieman, L. K. et al. Cushing syndrome. *Nat Rev Dis Primers* **11**, 4 (2025).
6. Dong, J., Hahner, S., Bancos, I. & Tomlinson, J. W. Clinical features, investigation, and management of Addison's disease. *Lancet Diabetes Endocrinol* **14**, 243-258 (2026).
7. Lyraki, R. & Schedl, A. Adrenal cortex renewal in health and disease. *Nat Rev Endocrinol* **17**, 421-434 (2021).
8. Teblick, A., Peeters, B., Langouche, L. & Van den Berghe, G. Adrenal function and dysfunction in critically ill patients. *Nat Rev Endocrinol* **15**, 417-427 (2019).
9. Valenza, G., Matic, Z. & Catrambone, V. The brain-heart axis: integrative cooperation of neural, mechanical and biochemical pathways. *Nat Rev Cardiol* **22**, 537-550 (2025).
10. Van Slycke, S., Van Den Heede, K. & Vandenwyngaerden, E.: Adrenal glands: Anatomy, physiology, and pathophysiology, in Endocrine Surgery Comprehensive Board Exam Guide. Edited by A.L. Shifrin, M. Raffaelli, G.W. Randolph & O. Gimm, Springer, Cham, 2021.
11. Navin, P. J. & Moynagh, M. R. Optimal and novel imaging of the adrenal glands. *Curr Opin Endocrinol Diabetes Obes* **29**, 253-262 (2022).
12. Johnson, P. T., Horton, K. M. & Fishman, E. K. Adrenal mass imaging with multidetector CT: pathologic conditions, pearls, and pitfalls. *Radiographics* **29**, 1333-1351 (2009).
13. Rubin, R. T. & Phillips, J. J. Adrenal gland volume determination by computed tomography and magnetic resonance imaging in normal subjects. *Invest Radiol* **26**, 465-469 (1991).
14. Geraghty, E. M., Boone, J. M., McGahan, J. P. & Jain, K. Normal organ volume assessment from abdominal CT. *Abdom Imaging* **29**, 482-490 (2004).
15. Wang, X. et al. Evaluation of normal adrenal gland volume by 64-slice CT. *Chin Med Sci J* **27**, 220-224 (2013).
16. Pacak, K. et al. Adrenal tumour imaging: clinical, molecular, and radiomics perspectives. *Lancet Diabetes Endocrinol* **14**, 62-81 (2026).
17. Velema, M. S. et al. Volumetric evaluation of CT images of adrenal glands in primary aldosteronism. *J Endocrinol Invest* **44**, 2359-2366 (2021).
18. Kim, T. M. et al. Fully automatic volume measurement of the adrenal gland on CT using deep learning to classify adrenal hyperplasia. *Eur Radiol* **33**, 4292-

4302 (2023).
19. Wang, F. et al. CT and MRI of adrenal gland pathologies. *Quant Imaging Med Surg* **8**, 853-875 (2018).
20. Nemeroff, C. B. et al. Adrenal gland enlargement in major depression. A computed tomographic study. *Arch Gen Psychiatry* **49**, 384-387 (1992).
21. Kessing, L. V., Willer, I. S. & Knorr, U. Volume of the adrenal and pituitary glands in depression. *Psychoneuroendocrinology* **36**, 19-27 (2011).
22. Liu, Y. et al. Adrenal limb thickness is associated with metabolism profiles in patients with diabetes: A cross-sectional study. *J Diabetes* **16**, e13479 (2024).
23. Li, Y. et al. Personalized adrenal gland volume reference ranges and development of a fully automated deep learning screening tool. *Eur J Radiol* **195**, 112591 (2026).
24. Wachinger, C., Renger, B., Spath, C. & Makowski, M. R. Body charts from CT segmentations across the adult lifespan: Large-scale cross-sectional and longitudinal analyses. *Radiol Artif Intell* **8**, e250506 (2026).
25. Liu, Y. et al. Genetic architecture of 11 organ traits derived from abdominal MRI using deep learning. *Elife* **10** (2021).
26. Bethlehem, R. A. I. et al. Brain charts for the human lifespan. *Nature* **604**, 525-533 (2022).
27. Zhuo, Z. et al. Charting brain morphology in international healthy and neurological populations. *Nat Neurosci* **29**, 420-434 (2026).
28. Li, J. et al. Morphometric brain organization across the human lifespan reveals increased dispersion linked to cognitive performance. *PLoS Biol* **22**, e3002647 (2024).
29. Chen, Y. et al. Age-related morphometrics of normal adrenal glands based on deep learning-aided segmentation. *Heliyon* **9**, e16810 (2023).
30. Schneller, J. et al. Linear and volumetric evaluation of the adrenal gland--MDCT-based measurements of the adrenals. *Acad Radiol* **21**, 1465-1474 (2014).
31. Montagne, J. P., Kressel, H. Y., Korobkin, M. & Moss, A. A. Computed tomography of the normal adrenal glands. *AJR Am J Roentgenol* **130**, 963-966 (1978).
32. Vincent, J. M., Morrison, I. D., Armstrong, P. & Reznek, R. H. The size of normal adrenal glands on computed tomography. *Clin Radiol* **49**, 453-455 (1994).
33. Wasserthal, J. et al. TotalSegmentator: Robust segmentation of 104 anatomic structures in CT images. *Radiol Artif Intell* **5**, e230024 (2023).
34. Fayemiwo, M. et al. A novel pipeline for adrenal gland segmentation: Integration of a hybrid post-processing technique with deep learning. *J Imaging Inform Med* **38**, 3698-3710 (2025).
35. Meng, F. et al. A deep learning algorithm for automated adrenal gland segmentation on non-contrast CT images. *BMC Med Imaging* **25**, 142 (2025).
36. Luo, G. et al. An optimized two-stage cascaded deep neural network for adrenal segmentation on CT images. *Comput Biol Med* **136**, 104749 (2021).
37. Barat, M. et al. Artificial intelligence in adrenal imaging: A critical review of current applications. *Diagn Interv Imaging* **104**, 37-42 (2023).

38. Abel, L. et al. Intra-individual reproducibility of automated abdominal organ segmentation-performance of totalsegmentator compared to human readers and an independent nnU-Net model. *J Imaging Inform Med* **38**, 1617-1627 (2025).
39. Chu, Y. et al. Adrenocortical stem cells in health and disease. *Nat Rev Endocrinol* **21**, 464-481 (2025).
40. Iwahashi, N. et al. Single-cell and spatial transcriptomics analysis of human adrenal aging. *Mol Metab* **84**, 101954 (2024).
41. Bechmann, N. et al. Asymmetric adrenals: Sexual dimorphism of adrenal tumors. *J Clin Endocrinol Metab* **109**, 471-482 (2024).
42. Lenzini, L., Caroccia, B., Seccia, T. M. & Rossi, G. P. Peptidergic G protein-coupled receptor regulation of adrenal function: Bench to bedside and back. *Endocr Rev* **43**, 1038-1050 (2022).
43. Saxu, R., Yang, Y. & Gu, H. F. Asymmetries of left and right adrenal glands in neural innervation and Glucocorticoids production. *Int J Mol Sci* **24** (2023).
44. Fu, R. et al. In situ spatial reconstruction of distinct normal and pathological cell populations within the human adrenal gland. *J Endocr Soc* **7**, bvad131 (2023).
45. Altieri, B. et al. Single-nucleus and spatial transcriptome reveal adrenal homeostasis in normal and tumoural adrenal glands. *Clin Transl Med* **14**, e1798 (2024).
46. Rood, J. E. et al. Toward a common coordinate framework for the human body. *Cell* **179**, 1455-1467 (2019).
47. Borner, K. et al. Anatomical structures, cell types and biomarkers of the Human Reference Atlas. *Nat Cell Biol* **23**, 1117-1128 (2021).
48. Rood, J. E. et al. The Human Cell Atlas from a cell census to a unified foundation model. *Nature* **637**, 1065-1071 (2025).
49. Chau, W. & McIntosh, A. R. The Talairach coordinate of a point in the MNI space: how to interpret it. *Neuroimage* **25**, 408-416 (2005).
50. Mazziotta, J. et al. A probabilistic atlas and reference system for the human brain: International Consortium for Brain Mapping (ICBM). *Philos Trans R Soc Lond B Biol Sci* **356**, 1293-1322 (2001).
51. Brett, M., Johnsrude, I. S. & Owen, A. M. The problem of functional localization in the human brain. *Nat Rev Neurosci* **3**, 243-249 (2002).
52. William D. Penny, Karl J. Friston, John T. Ashburner, Stefan J. Kiebel & Nichols, T. E. Statistical Parametric Mapping: The Analysis of Functional Brain Images. (2006).
53. Poldrack, R. A. & Farah, M. J. Progress and challenges in probing the human brain. *Nature* **526**, 371-379 (2015).
54. Rorden, C. MRIcroGL: voxel-based visualization for neuroimaging. *Nat Methods* **22**, 1613-1614 (2025).
55. Rorden, C. Surfice: visualizing neuroimaging meshes, tractography streamlines and connectomes. *Nat Methods* **22**, 1615-1616 (2025).
56. Casamitjana, A. et al. A probabilistic histological atlas of the human brain for

MRI segmentation. *Nature* **648**, 678-685 (2025).
57. Amunts, K., Mohlberg, H., Bludau, S. & Zilles, K. Julich-Brain: A 3D probabilistic atlas of the human brain's cytoarchitecture. *Science* **369**, 988-992 (2020).
58. Hawrylycz, M. J. et al. An anatomically comprehensive atlas of the adult human brain transcriptome. *Nature* **489**, 391-399 (2012).
59. Bai, W. et al. A bi-ventricular cardiac atlas built from 1000+ high resolution MR images of healthy subjects and an analysis of shape and motion. *Med Image Anal* **26**, 133-145 (2015).
60. G. R. De Luca, M. Mascalchi & S. Diciotti: Development of a 3-D standardized lung template from low-dose CT scans, in 2025 IEEE EMBS International Conference on Biomedical and Health Informatics (BHI), Atlanta, GA, USA2025, 2025, pp.
61. Yayon, N. et al. A spatial human thymus cell atlas mapped to a continuous tissue axis. *Nature* **635**, 708-718 (2024).
62. Ahmad, N. et al. Voxel-wise body composition analysis using image registration of a three-slice CT imaging protocol: methodology and proof-of-concept studies. *Biomed Eng Online* **23**, 42 (2024).
63. Lind, L., Strand, R., Michaelsson, K., Ahlstrom, H. & Kullberg, J. Voxel-wise study of cohort associations in whole-body MRI: Application in metabolic syndrome and its components. *Radiology* **294**, 559-567 (2020).
64. Borner, K. et al. Human biomolecular atlas program (HuBMAP): 3D human reference atlas construction and usage. *Nat Methods* **22**, 845-860 (2025).
65. Hu, B. C. The human body at cellular resolution: the NIH human biomolecular atlas program. *Nature* **574**, 187-192 (2019).
66. Jain, S. et al. Advances and prospects for the Human BioMolecular Atlas Program (HuBMAP). *Nat Cell Biol* **25**, 1089-1100 (2023).
67. Landman, B. et al.: Miccai multi-atlas labeling beyond the cranial vault–workshop and challenge, in he MICCAI Multi-Atlas Labeling Beyond Cranial Vault — Workshop Challenge, Workshop Challenge, Munich, German2015, 2015, pp.
68. Holz, N. E. et al. A stable and replicable neural signature of lifespan adversity in the adult brain. *Nat Neurosci* **26**, 1603-1612 (2023).
69. Evans, A. C., Janke, A. L., Collins, D. L. & Baillet, S. Brain templates and atlases. *Neuroimage* **62**, 911-922 (2012).
70. Lind, L., Kullberg, J., Ahlstrom, H., Michaelsson, K. & Strand, R. Proof of principle study of a detailed whole-body image analysis technique, "Imiomics", regarding adipose and lean tissue distribution. *Sci Rep* **9**, 7388 (2019).
71. Strand, R. et al. A concept for holistic whole body MRI data analysis, Imiomics. *PLoS One* **12**, e0169966 (2017).
72. John, R. et al. Normal adrenal gland thickness on computerized tomography in an Asian Indian adult population. *Indian J Radiol Imaging* **28**, 465-469 (2018).
73. Consortium, M. et al. MRI-based multi-organ clocks for healthy aging and disease assessment. *Nat Med* **32**, 82-92 (2026).
74. Zhao, B. et al. Heart-brain connections: Phenotypic and genetic insights from

magnetic resonance images. *Science* **380**, abn6598 (2023).
75. Shu, J. et al. Inferring multi-organ genetic connections using imaging and clinical data through Mendelian randomization. *Nat Biomed Eng* (2025).
76. Ashburner, J. & Friston, K. J. Voxel-based morphometry--the methods. *Neuroimage* **11**, 805-821 (2000).
77. Tezuka, Y. et al. The age-dependent changes of the human adrenal cortical zones are not congruent. *J Clin Endocrinol Metab* **106**, 1389-1397 (2021).
78. Gao, X. et al. Gender differences in human adrenal cortex and its disorders. *Mol Cell Endocrinol* **526**, 111177 (2021).
79. Nonaka, K. et al. Correlation between telomere attrition of zona fasciculata and adrenal weight reduction in older men. *J Clin Endocrinol Metab* **105**, dgz214 (2020).
80. Chen, Y. et al. Sex difference in adrenal developmental toxicity induced by dexamethasone and its intrauterine programming mechanism. *Pharmacol Res* **174**, 105942 (2021).
81. Ludescher, B. et al. Gender specific correlations of adrenal gland size and body fat distribution: a whole body MRI study. *Horm Metab Res* **39**, 515-518 (2007).
82. Liu, F. et al. Obesity might persistently increase adrenal gland volume: a preliminary study. *Obes Surg* **30**, 3503-3507 (2020).
83. Wang, W. et al. Neutrophil-lymphocyte ratio as an initial screening biomarker for differential diagnosis of Cushing's syndrome from nonfunctional adenoma in patients with an adrenal mass. *Biomed Res Int* **2021**, 6635594 (2021).
84. Askani, E. et al. MRI-based adrenal gland volume is associated with cardiovascular alterations in individuals without prior cardiovascular disease. *Sci Rep* **14**, 14664 (2024).
85. Kahl, K. G. et al. Adrenal gland volume, intra-abdominal and pericardial adipose tissue in major depressive disorder. *Psychoneuroendocrinology* **58**, 1-8 (2015).
86. Szigethy, E., Conwell, Y., Forbes, N. T., Cox, C. & Caine, E. D. Adrenal weight and morphology in victims of completed suicide. *Biol Psychiatry* **36**, 374-380 (1994).
87. Stepansky, L. et al. Adrenal gland volume measurement in depressed patients. *J Psychiatr Res* **187**, 74-79 (2025).
88. Isensee, F., Jaeger, P. F., Kohl, S. A. A., Petersen, J. & Maier-Hein, K. H. nnU-Net: a self-configuring method for deep learning-based biomedical image segmentation. *Nat Methods* **18**, 203-211 (2021).
89. Avants, B. B., Epstein, C. L., Grossman, M. & Gee, J. C. Symmetric diffeomorphic image registration with cross-correlation: evaluating automated labeling of elderly and neurodegenerative brain. *Med Image Anal* **12**, 26-41 (2008).
90. Johnson, W. E., Li, C. & Rabinovic, A. Adjusting batch effects in microarray expression data using empirical Bayes methods. *Biostatistics* **8**, 118-127 (2007).
91. Sun, L. et al. Human lifespan changes in the brain's functional connectome. *Nat Neurosci* **28**, 891-901 (2025).
92. Ge, R. et al. Normative modelling of brain morphometry across the lifespan with CentileBrain: algorithm benchmarking and model optimisation. *Lancet Digit Health* **6**, e211-e221 (2024).

93. Midzak, A. & Papadopoulos, V. Adrenal mitochondria and steroidogenesis: From individual proteins to functional protein assemblies. *Front Endocrinol (Lausanne)* **7**, 106 (2016).

Figure Legends

Figure 1.

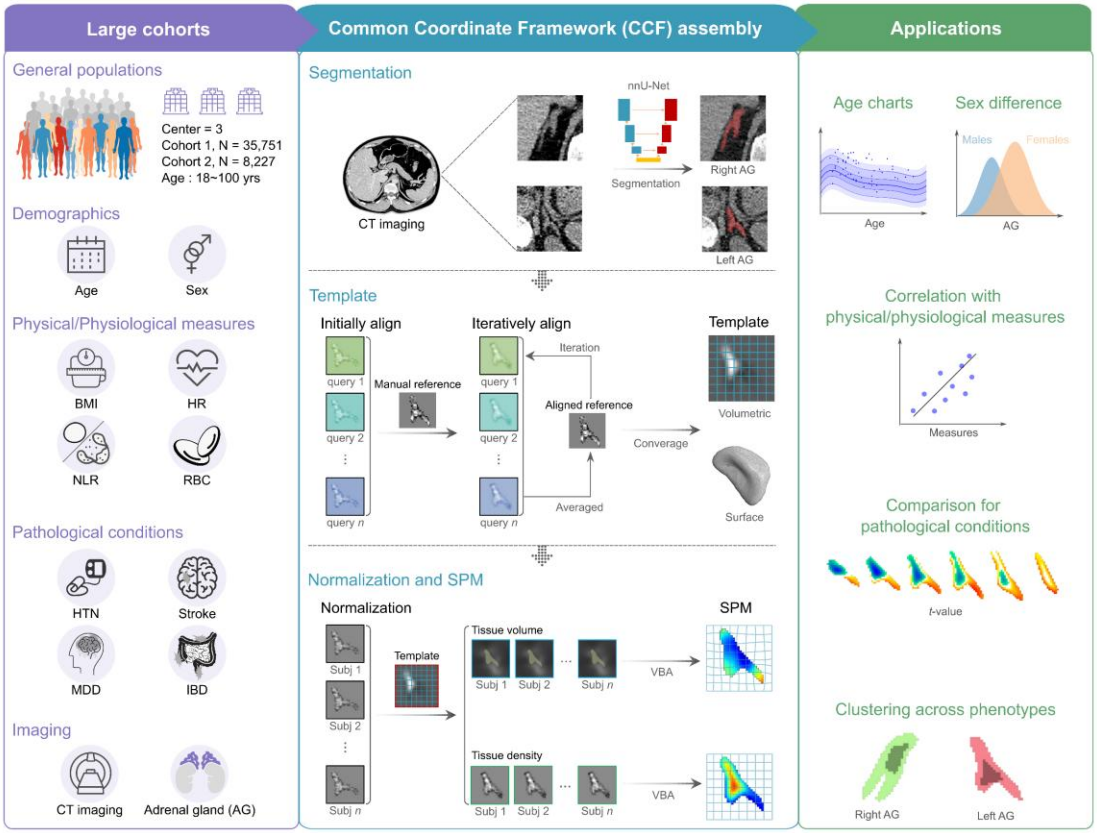


Figure 1. Study design. (*Left panel***)** We employed chest Computed Tomography (CT) imaging data from large-cohort participants (*N* = 37,251) aged 18 to 100 years across three centers. Available physical and physiological measures included body mass index (BMI), heart rate (HR), neutrophil-to-lymphocyte ratio (NLR), and red blood cell count (RBC). We examined four pathological conditions: hypertension (HTN), stroke, major depressive disorder (MDD), and inflammatory bowel disease (IBD). **(***Middle panel***)** To construct a common coordinate framework for adrenal glands, we first developed a nnU-Net model to segment adrenal glands across 300 queries. We constructed a three-dimensional standard adrenal template on 1,338 individuals. And then, each individual's adrenal glands were normalized to bilateral adrenal gland templates within a common coordinate framework (CCF), which enabled us to subsequently perform voxel-based analysis (VBA). Based on the CCF-adrenal glands, we obtained each individual's adrenal gland density and volume *per* voxel, which were then used for a Statistical Parametric Mapping (SPM). **(***Right panel***)** We depicted age-related changes in adrenal gland density and volume, explored associations between

physical/physiological measures and abnormal patterns of pathological conditions, and investigated age-related changes in the inner and outer adrenal glands.

Figure 2.

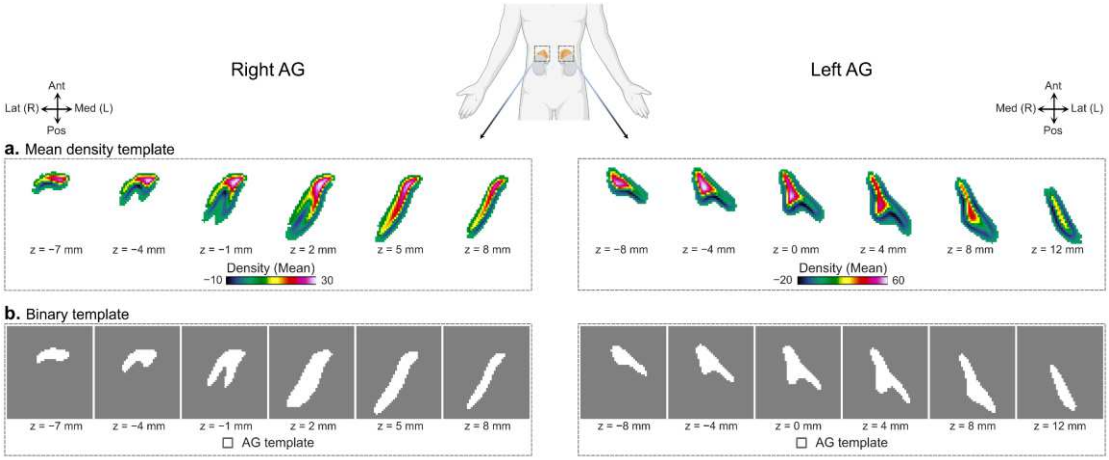


Figure 2. Views of bilateral adrenal gland templates within CCF. a, The spatial distribution of mean density for bilateral adrenal glands. **b,** The view of binary adrenal gland templates.

Figure 3.

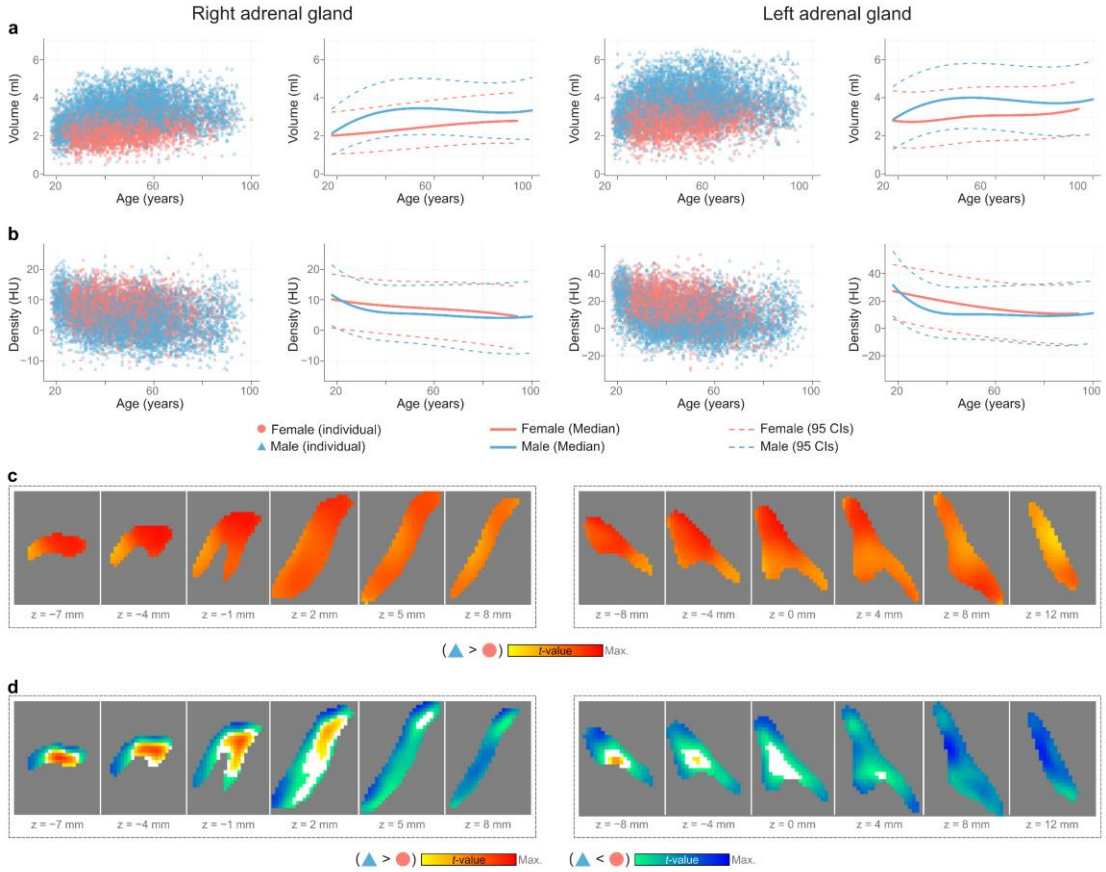


Figure 3. Charts of adrenal volume and density across the lifespan and between sexes in CCF. a & b, Age trajectories of right and left adrenal gland volume and density from 18 to 100 years, shown separately for males (blue) and females (red). Dotted lines indicate 95% confidence intervals. **c & d,** Voxel-wise sex differences in adrenal volume and density. Red bars indicate regions with significantly higher values in males than in females; blue bars indicate regions with significantly lower values in males.

Figure 4.

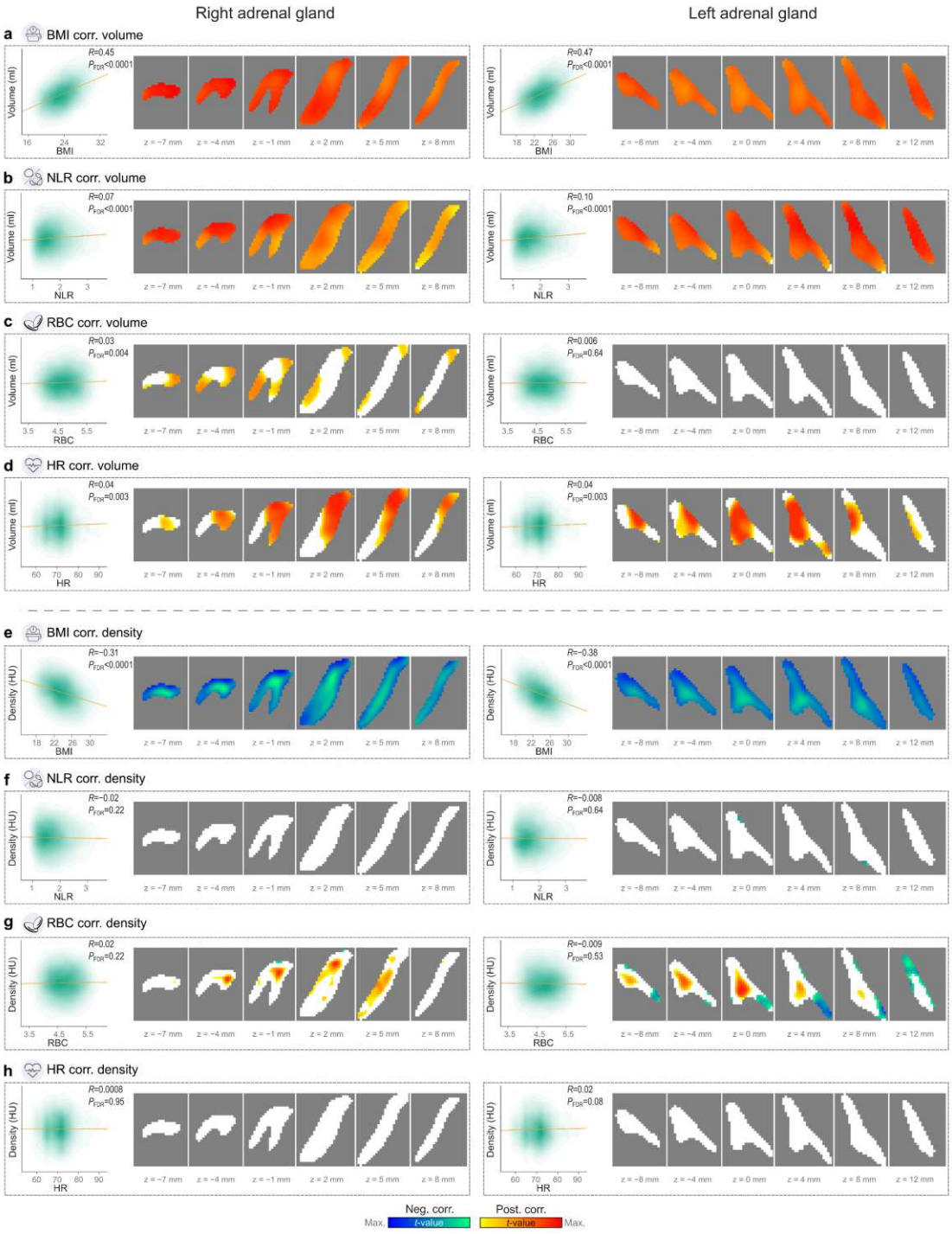


Figure 4. Statistical parametric mapping of adrenal gland by correlating imaging metrics and physical/physiological measures. a-d, Whole-gland and voxel-wise associations of adrenal volume with body mass index (BMI), neutrophil-to-lymphocyte ratio (NLR), red blood cell count (RBC), and heart rate (HR). **e-h,** Whole-gland and voxel-wise associations of adrenal density with BMI, NLR, RBC, and HR. Red bars indicate positive associations; blue bars indicate negative associations. All *P*-values <

0.05 and corrected by false discovery rate (FDR).

Figure 5.

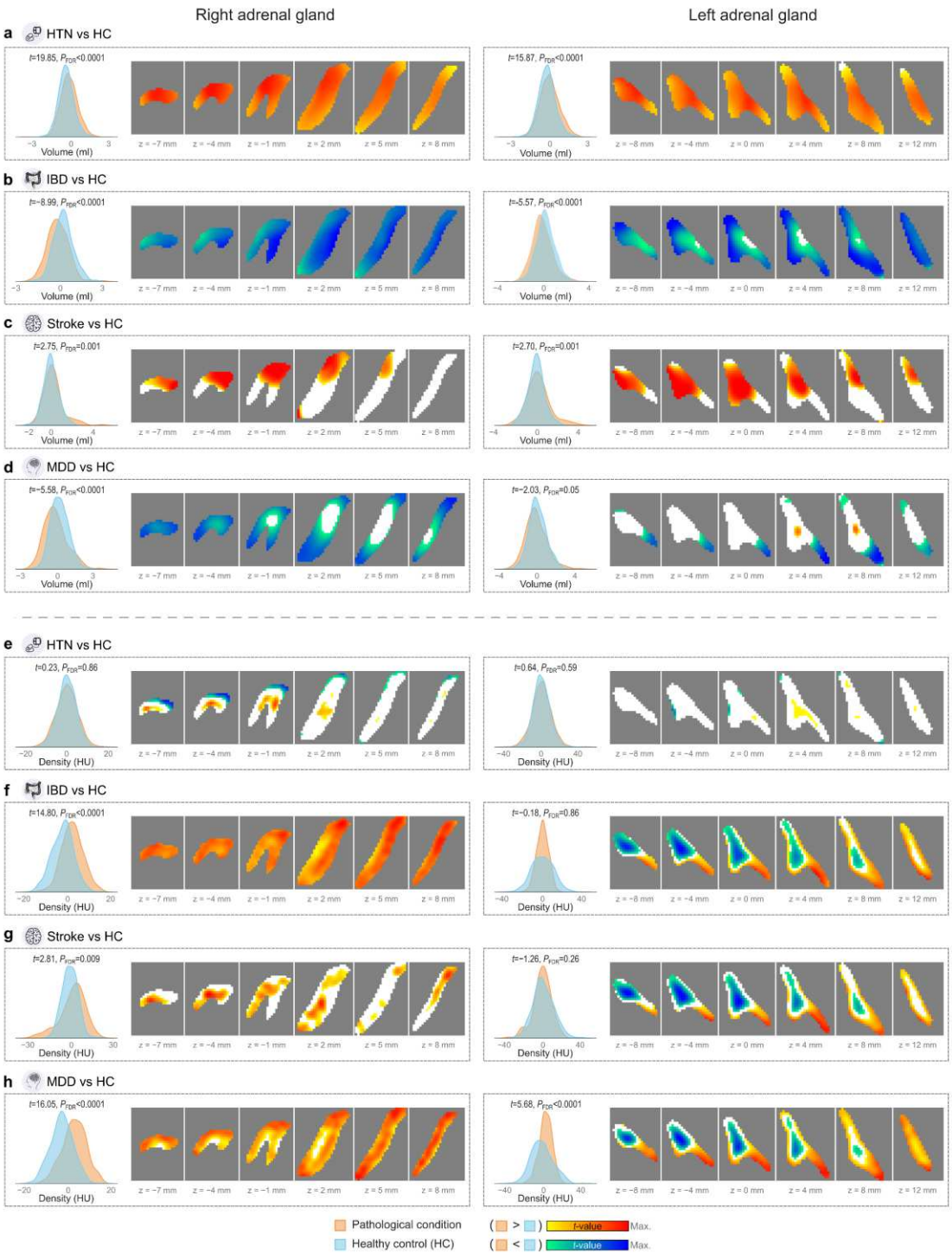


Figure 5. Changed patterns of adrenal metrics in four pathological conditions. a-d, Significant whole-gland and voxel-wise changes in adrenal volume in individuals with hypertension (HTN), inflammatory bowel disease (IBD), stroke, and major depressive disorder (MDD) against HCs. **e-h,** S Significant whole-gland and voxel-wise abnormalities in adrenal density in individuals with HTN, IBD, stroke, and MDD relative

to HCs. Red bars indicate significant increases and blue bars significant decreases in patient groups compared to HCs. All results were corrected using FDR at $P < 0.05$.

Supplementary Files

This is a list of supplementary files associated with this preprint. Click to download.

- Supplementarymaterialsv13WL.docx